NANO LETTERS

pubs.acs.org/NanoLett

Letter

Integrated Molar Chiral Sensing Based on High-*Q* Metasurface

Yang Chen, Chen Zhao, Yongzhe Zhang, and Cheng-wei Qiu*

Cite This: *Nano Lett.* 2020, 20, 8696–8703

Read Online

ACCESS | Metrics & More | Article Recommendations | Supporting Information

ABSTRACT: Circular dichroism (CD) spectroscopy is conventionally utilized for the enantiomer-specific analysis of chiral samples, which is of great significance in academia and industry. Recently, metasurfaces have been introduced for enhancing the sensitivity of CD spectroscopy. However, the obtained CD spectrum alone cannot provide the enantiomer composition of a chiral sample. It should be normalized by the molar concentration of chiral molecules, which is usually measured on a different platform. Here, for the first time we demonstrate the integrated acquisition of CD spectrum and molar concentration over an individual metasurface with high sensitivities. High-Q resonances are supported on the metasurface, governed by bound states in the continuum. The generated superchiral field enables a 59-times enhancement of CD signal. Meanwhile, the refractive index-based detection of molar concentration achieves a large figure-of-merit of 80.6. Accordingly, a standard procedure is established for the integrated molar chiral sensing with high sensitivity.

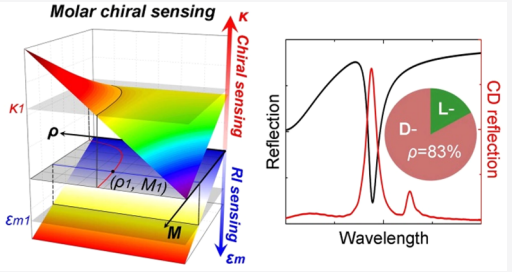

KEYWORDS: *optical chirality, molar circular dichroism, bound states in the continuum, hybrid metasurface, biosensing*

Chirality plays an essential role in life. It refers to the geometric symmetry property of an object without any mirror symmetry or inversion symmetry. Many of the fundamental biomolecules, such as amino acids, nucleic acids and carbohydrates, exist in two enantiomer forms that are mirror images of each other.[1] Since the two enantiomers (say D- and L-) may exhibit totally different biochemical properties and functions, the analysis of enantiomer composition is of great importance in food industry,[2] medical diagnostics,[3] and drug development.[4]

Circular dichroism (CD) spectroscopy is usually employed for enantiomer analysis, where the absorption difference of right- and left-handed circularly polarized (RCP and LCP) light by chiral molecules is calculated as $\Delta A = A_R - A_L$. However, the CD spectrum alone cannot give the enantiomer composition of a sample. It should be normalized by scaling to the molar concentration of chiral molecules M (unit: mol/cm^3)[5,6]

$$\Delta A_{molar} = \frac{\Delta A}{(M \cdot l)} \tag{1}$$

where l is the path length of light through the sample. Currently, in order to extract molar CD ΔA_{molar}, CD spectrum and molar concentration are usually measured by different apparatus. There is an urgent need for the simultaneous measurement of the two quantities over an individual platform.

The conventional CD spectroscopy for enantiomer analysis usually suffers from low sensitivity, caused by the scale mismatch between the helical pitch of chiral molecules and light wavelength. Recently, metasurfaces have been extensively proposed for enhanced chiral sensing,[7−19] because they can squeeze the electromagnetic field into the subwavelength volumes and generate superchiral fields with enhanced local density of chirality. However, all the existing works only acquire the CD spectra of chiral samples, based on which the enantiomer composition cannot be derived due to the lack of molecular concentration. As illustrated in Figure 1a, the three chiral samples can exhibit identical CD intensity, even though they have distinct enantiomer ratios $\rho = M_D/(M_D + M_L)$, where M_D and M_L are the molar concentrations of D- and L-molecules. Thus, it is necessary to also measure the total molar concentration of chiral molecules in the sample. This task can be fulfilled by another class of nanophotonic biosensors,[20−24] which are able to detect the variation of refractive index (RI) through the spectral shift of optical resonance. By integrating the functions of chiral sensing and RI sensing onto an individual metasurface, molar chiral sensing can be realized for the analysis of enantiomer composition, which, to our knowledge, has never been demonstrated before. Besides, the sensitivity of molar chiral sensing is cooperatively determined by the sensitivities of chiral sensing and RI sensing, both of which are strongly related to the quality factor (q-factor) of optical resonance. Therefore, achieving high q-factor in metasurface is critical for high-sensitivity molar chiral sensing, which can be realized based on the physics of bound states in

Received: August 31, 2020
Revised: October 14, 2020
Published: November 20, 2020

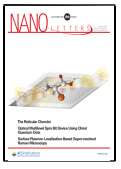

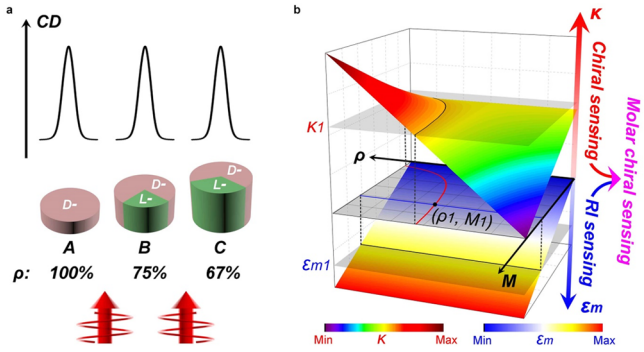

Figure 1. Concept of molar chiral sensing. (a) Three chiral samples (*A*, *B*, *C*) with different enantiomer ratios ρ exhibiting identical CD intensity. Their molar concentrations as represented by the volumes are different. (b) The values of ε_m and κ form two surfaces in the parameter space of ρ and *M*. Chiral sensing and RI sensing can respectively determine the values of ε_m and κ, which, in turn, give rise to two data lines in the ρ-*M* plane. Molar chiral sensing, as a combination of chiral sensing and RI sensing, is to search the intersection point of the two lines, and get the certain values of ρ and *M*.

the continuum (BIC). A true photonic BIC represents an optical mode with an infinitely large *q*-factor, and a perturbation can evolve a BIC to a quasi-BIC still possessing a high *q*-factor.[25−28]

In this work, we demonstrate, for the first time, the realization of integrated molar chiral sensing with enhanced sensitivity based on a high-*Q* metasurface. Benefiting from the simultaneous excitation of *x*- and *y*-polarized quasi-BIC modes with well-matched field distributions, a strong superchiral field is generated around the metasurface, leading to a 59-times enhancement of the CD reflection signal from the chiral sample. The Pasteur parameter κ can thus be retrieved with enhanced sensitivity. Also, the high-*Q* quasi-BIC mode empowers the sensitive RI-based detection of molar concentration *M* with a large figure-of-merit (FOM) of 80.6. Then, the enantiomer ratio ρ of the test sample can be derived based on the information on κ and *M*. Finally, a standard procedure is proposed for the rapid, accurate, and convenient analysis of enantiomer composition, which, we believe, can find wide applications in food industry, disease diagnostics, and drug development.

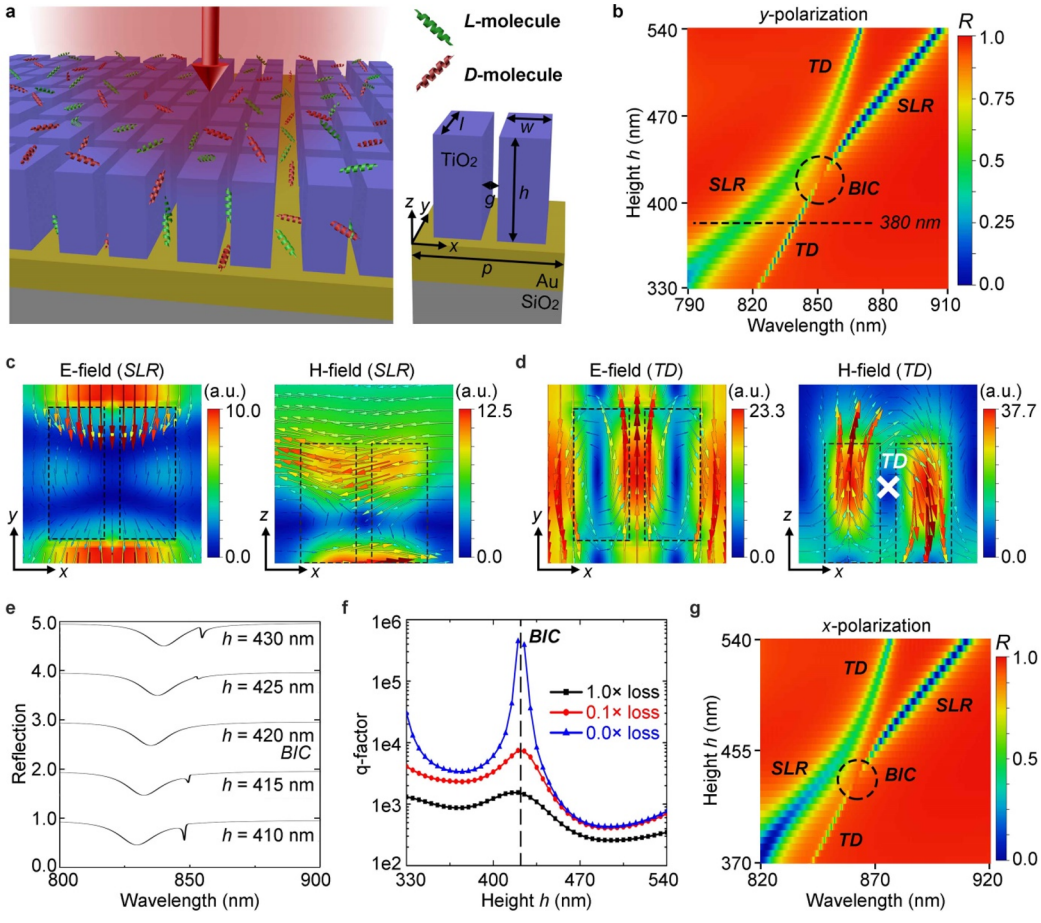

Figure 2. BIC formation in the metasurface. (a) Schematic of the hybrid metasurface with chiral molecules deposited on the surface. The unit-cell structure is illustrated on the right. (b) Simulated reflection spectra for different dimer height *h* under *y*-polarized normal incidence. The two mode branches are indicated, while the formation of BIC is marked by a dashed circle. (c,d) Normalized electric and magnetic field distributions inside a unit cell (*h* = 380 nm) for the SLR mode (c) and TD mode (d). (e) Reflection spectra for different height *h* around the BIC condition. (f) Extracted *q*-factors for the quasi-BIC mode with different height *h*. To suppress the nonradiative decay channel, the imaginary part of material permittivity can be reduced from the original value (1.0× loss) to one tenth of it (0.1× loss) or zero (0× loss). The *q*-factor is divergent at the BIC condition (dashed line) for the zero loss case. (g) Simulated reflection spectra for different dimer height *h* under *x*-polarized normal incidence.

https://dx.doi.org/10.1021/acs.nanolett.0c03506
Nano Lett. 2020, 20, 8696−8703

Basically, the chiral sample can be modeled as a homogeneous layer, whose constitutive relationships are expressed as

$$\mathbf{D} = \varepsilon_m \mathbf{E} + \frac{i\kappa \mathbf{H}}{c} \tag{2}$$

$$\mathbf{B} = \mu_m \mathbf{H} - \frac{i\kappa \mathbf{E}}{c} \tag{3}$$

where ε_m and μ_m are the permittivity and permeability, and κ is the Pasteur parameter describing its chiral property. For natural chiral materials, μ_m is equal to one, while ε_m and κ are associated with the molecular electronic transitions, which are expressed as[29,30]

$$\varepsilon_m = \varepsilon_{m,0} - \frac{4}{3}\pi\left(\frac{1}{\hbar\omega - \hbar\omega_0 + i\Gamma_{12}} - \frac{1}{\hbar\omega + \hbar\omega_0 + i\Gamma_{12}}\right) M \cdot N_A |\boldsymbol{\mu}_{12}|^2 \tag{4}$$

$$\kappa = \frac{4}{3} i\pi\left(\frac{1}{\hbar\omega - \hbar\omega_0 + i\Gamma_{12}} + \frac{1}{\hbar\omega + \hbar\omega_0 + i\Gamma_{12}}\right) M \cdot N_A (\mu_{12} \cdot m_{21}) \tag{5}$$

Here, $\varepsilon_{m,0}$ is the background permittivity; ω_0 and Γ_{12} are the angular frequency and broadening of resonant transition, respectively; N_A is the Avogadro constant; μ_{12} and m_{21} are the electric and magnetic dipole matrix elements for the molecular transition (see Supporting Information S2). We can see that a nonzero scalar product $(\mu_{12} \cdot m_{21})$ is the key for optical activity, and this scalar product usually possesses opposite signs for opposite enantiomers. For a chiral sample with an enantiomer ratio ρ, the expressions of ε_m and κ can be rewritten as

$$\varepsilon_m = \varepsilon_{m,0} + A \cdot M \tag{6}$$

$$\kappa = (2\rho - 1) B \cdot M \tag{7}$$

where A and B are parameters related to the electronic transitions and are specific to the molecular species. According to eqs 6 and 7, two surfaces, corresponding to ε_m and κ, are formed in the parameter space of ρ and M (Figure 1b). When a certain κ_1 is acquired for a test sample by chiral sensing, a group of data points (ρ_1, M_1) are retrieved forming a curved line, and the exact values of ρ and M are still unknown. Similarly, the acquisition of $\varepsilon_{m,1}$ by RI sensing results in a straight line in the $\rho-M$ plane. The task of molar chiral sensing is to search the intersection point of the two lines and to uniquely determine the values of ρ and M.

The metasurface for integrated molar chiral sensing is composed of an array of titanium dioxide (TiO_2) dimers sitting on an optically thick gold film (Figure 2a), which could be fabricated based on electron beam lithography (EBL) followed by atomic layer deposition (ALD) process.[31] The background medium on top of the metasurface is assumed to be water (RI = 1.33), and the chiral sample is deposited with a thickness of t = 20 nm. The reflection spectra of the metasurface under y-polarized normal incidence is simulated for different dimer height h, while the in-plane geometric parameters are fixed (p = 560 nm, w = 180 nm, l = 420 nm, g = 40 nm). As shown in Figure 2b, two mode branches are resolved, which undergo a strong coupling accompanied by a typical avoided crossing behavior. The Rabi splitting is calculated to be 23 meV, which is larger than the average dissipation rate of the two modes, fulfilling the criterion of strong coupling (see Supporting Information S3). At a certain point around the crossing regime, the spectral width of one branch entirely vanishes, indicating the formation of BIC.[32] This BIC belongs to the Friedrich-Wintgen (or accidental) BIC and it results from the destructive interference between the two leaky modes. The origin of the two modes is examined at h = 380 nm. The broadband high-energy resonance at 812.2 nm is attributed to surface lattice resonance (SLR) because it exhibits typical field patterns of SLR (Figure 2c).[33] As to the narrowband low-energy resonance at 838.5 nm, it is attributed to the electric toroidal dipole (simplified as toroidal dipole (TD) in the following) mode,[34,35] where the electric field is circulating on the surface of a torus along its meridians and the magnetic field is flowing along a closed loop in the xz plane (Figure 2d). The generated TD is pointed to the $+y$ direction along the symmetry axis of the torus. Multipolar decomposition is performed to further confirm the TD origin of this mode (see Supporting Information S4). In general, the TD mode is supported by separate nanoresonators with high-index materials, and the mode field is dominantly confined inside the nanoresonators.[34−37] However, for this metasurface the TiO_2 nanobricks are closely packed, leading to strong inter- and intradimer near-field coupling. Such lattice effects play a key role in the excitation of the TD mode. As a result, the electric field is mainly distributed outside the nanobricks and can be accessed by the surrounding chiral molecules, which is important for enhanced biosensing.[15] Another key factor for the BIC formation is the presence of gold substrate. On one hand, the surface plasmon currents within the gold film is important for the excitation of SLR resonance in this metasurface.[33] On the other hand, the gold substrate can help bring the two mode branches together and promote their strong coupling via the bianisotropy response[38] (see Supporting Information S5).

When the parameter h is deviated from the BIC condition, a sharp, asymmetric Fano line shape is observed (Figure 2e), which is recognized as the quasi-BIC mode.[27] Such a Fano line shape becomes broader and more prominent as h moves away from the BIC condition, suggesting an enhanced coupling to the radiation continuum. Eigenmode analysis is conducted to extract the q-factors of quasi-BICs. As shown in Figure 2f, the q-factor reaches the maximum value of 1540 at the BIC condition. Generally, the total q-factor Q consists of a radiative part Q_r and a nonradiative part Q_{nr} via $1/Q = 1/Q_r + 1/Q_{nr}$.[32] Because of the existence of Ohmic loss, the BIC of this hybrid nanosystem possesses a finite q-factor determined by the nonradiative process, which is distinguished from those all-dielectric BIC systems with infinite q-factors. In simulations, the nonradiative decay channel can be suppressed by arbitrarily reducing the imaginary part of the material permittivity. Then, the q-factor is substantially boosted for the one-tenth loss case and is finally divergent for the zero loss case (Figure 2f). Similarly, a Friedrich-Wintgen BIC is also supported by the hybrid metasurface under x-polarized normal incidence (Figure 2g). Detailed analysis is provided in Supporting Information S6.

Quasi-BIC modes are well suited for the application of biosensing due to the large near-field enhancement and high q-factor. When the metasurface is illuminated with circularly polarized light (CPL), the two quasi-BICs for x- and y-polarized light are simultaneously excited, leading to the generation of superchiral fields. The h-dependent reflection spectra for circularly polarized incidence are demonstrated in Supporting Information S7. The chiral asymmetry in the excitation rate of chiral molecules can be substantially

https://dx.doi.org/10.1021/acs.nanolett.0c03506
Nano Lett. 2020, 20, 8696−8703

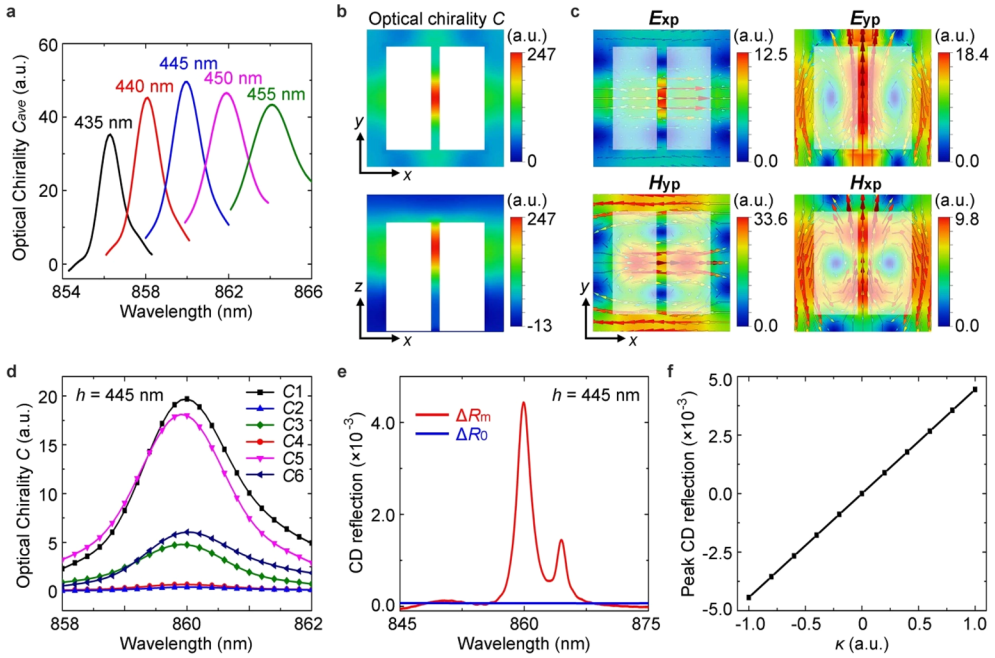

Figure 3. Chiral sensing empowered by quasi-BICs. (a) Normalized averaged optical chirality C_{ave} for different dimer height h. (b) Resonant optical chirality distributions at $x-y$ plane (top) and $x-z$ plane (bottom) in a unit cell (h = 445 nm). (c) In-plane electric and magnetic field distributions in a unit cell (h = 445 nm) for x- ($\mathbf{E}_{xp}$ and $\mathbf{H}_{xp}$) and y-polarized ($\mathbf{E}_{yp}$ and $\mathbf{H}_{yp}$) incidence at the C_{ave} resonance, showing well-matched field patterns. (d) Cartesian decomposition of the optical chirality into six components ($C1$ to $C6$). (e) Simulated CD reflection spectrum of a chiral layer deposited on the metasurface (ΔR_m), along with a referenced CD reflection spectrum coming from a bare free-standing chiral layer of 150 nm thickness (ΔR_0). (f) Peak value of CD reflection spectrum as a function of κ, showing a linear relationship. Here, κ is normalized by the κ value of ρ = 100%.

enhanced by superchiral fields, which is commonly evaluated by the optical chirality C defined as[39,40]

$$C = -\frac{\omega}{2c^2} Im(\mathbf{E}^* \cdot \mathbf{H}) \tag{8}$$

We calculate the average optical chirality over the volume of chiral sample and then normalize it by the optical chirality of CPL. As shown in Figure 3a, the normalized averaged optical chirality C_{ave} can be up to 50.0 for h = 445 nm, which is larger than most of the previous results.[11,12,15,18,41] For this case, the optical chirality field is globally strong and predominantly positive around the metasurface. A hotspot is distributed in the gap area with a giant C value of 247 (Figure 3b). Compared to the existing nanophotonic platforms made of high-index materials,[12−15] the optical chirality field here is dominantly distributed outside the nanostructures due to the lattice effects and can be accessed by chiral molecules. Since the metasurface is structurally achiral, eq 8 can be rewritten to

$$\begin{aligned} C &= -\frac{\omega}{2c^2} \mathrm{Im}[(\mathbf{E}_{xp}^* + \mathbf{E}_{yp}^* \exp^{-i\varphi}) \cdot (\mathbf{H}_{xp} + \mathbf{H}_{yp} \exp^{i\varphi})] \\ &= -\frac{\omega}{2c^2} \mathrm{Im}(\mathbf{E}_{xp}^* \cdot \mathbf{H}_{yp} \exp^{i\varphi} + \mathbf{E}_{yp}^* \cdot \mathbf{H}_{xp} \exp^{-i\varphi}) \end{aligned} \tag{9}$$

where $\mathbf{E}_{xp}$ ($\mathbf{H}_{xp}$) and $\mathbf{E}_{yp}$ ($\mathbf{H}_{yp}$) are the electric (magnetic) field vectors induced by x- and y-polarized light, and φ is equal to $\pi/2$ and $-\pi/2$ for LCP and RCP illuminations. According to eq 9, large optical chirality is expected when $\mathbf{E}_{xp}$ and $\mathbf{H}_{yp}$, as well as $\mathbf{E}_{yp}$ and $\mathbf{H}_{xp}$, are strong, overlapped, and spatially paralleled with a $\pm\pi/2$ phase difference. Thus, we inspect the electric and magnetic field distributions for x- and y-polarized incidence at the C_{ave} resonance. As depicted in Figure 3c, both electric and magnetic fields are significantly enhanced around the metasurface, especially in the gap area. Meanwhile, $\mathbf{E}_{xp}$ and $\mathbf{H}_{yp}$, as well as $\mathbf{E}_{yp}$ and $\mathbf{H}_{xp}$, are globally overlapped and paralleled, fulfilling the requirement for large optical chiral generation. Here, the electric and magnetic field distributions clearly indicate the excitation of x- and y-polarized quasi-BIC modes, by comparing with the mode patterns in Figure 2d and Figure S5a. It is noted that the y-polarized quasi-BIC mode is resonantly excited with stronger field enhancement than that of the x-polarized quasi-BIC, which is off-resonant at this wavelength (see Supporting Information S8).

Further, we decompose the field vectors in eq 9 into the three Cartesian coordinates as

$$\begin{aligned} C &= -\frac{\omega}{2c^2} \mathrm{Im}(E_{x,xp}^* H_{x,yp} \exp^{i\varphi} + E_{y,xp}^* H_{y,yp} \exp^{i\varphi} + E_{z,xp}^* H_{z,yp} \exp^{i\varphi} \\ &\quad + E_{x,yp}^* H_{x,xp} \exp^{-i\varphi} + E_{y,yp}^* H_{y,xp} \exp^{-i\varphi} + E_{z,yp}^* H_{z,xp} \exp^{-i\varphi}) \\ &= C1 + C2 + C3 + C4 + C5 + C6, \end{aligned} \tag{10}$$

where $E_{x,yp}$ ($H_{x,yp}$) denotes the x-polarized electric (magnetic) field induced by y-polarized incidence, and the other notations are defined in the same way. By calculating and averaging the six components over the chiral volume, it is observed that the components $C1$ ($\sim E^*_{x,xp} H_{x,yp}$) and $C5$ ($\sim E^*_{y,yp} H_{y,xp}$) make a major contribution to the overall optical chirality C_{ave}, which is consistent with the field distributions in Figure 3c. Therefore, the strong superchiral fields originated from the on-resonant excitation of y-polarized quasi-BIC and the off-resonant excitation of x-polarized quasi-BIC with well-matched field distributions.

When chiral molecules are immersed in the superchiral field, the CD reflection spectrum, defined as the difference between the reflection spectra of RCP and LCP incidence $\Delta R_m = R_{RCP} - R_{LCP}$, is anticipated to be enhanced, which can be simulated by finite element method (Comsol Multiphysics). Here, we

https://dx.doi.org/10.1021/acs.nanolett.0c03506
Nano Lett. 2020, 20, 8696−8703

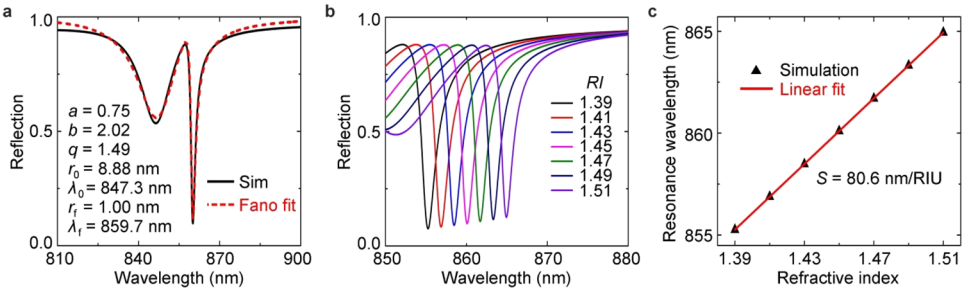

Figure 4. Sensitive detection of RI. (a) Simulated reflection spectrum of the metasurface (h = 445 nm) under y-polarized incidence, which is fitted by the analytical function of Fano resonance. The fitting parameters are listed. (b) Reflection spectra of the quasi-BIC mode (h = 445 nm) for different RI values of the chiral layer. (c) Resonant wavelength of the quasi-BIC as a function of RI, showing a linear dependence. The sensitivity is derived to be S = 80.6 nm/RIU.

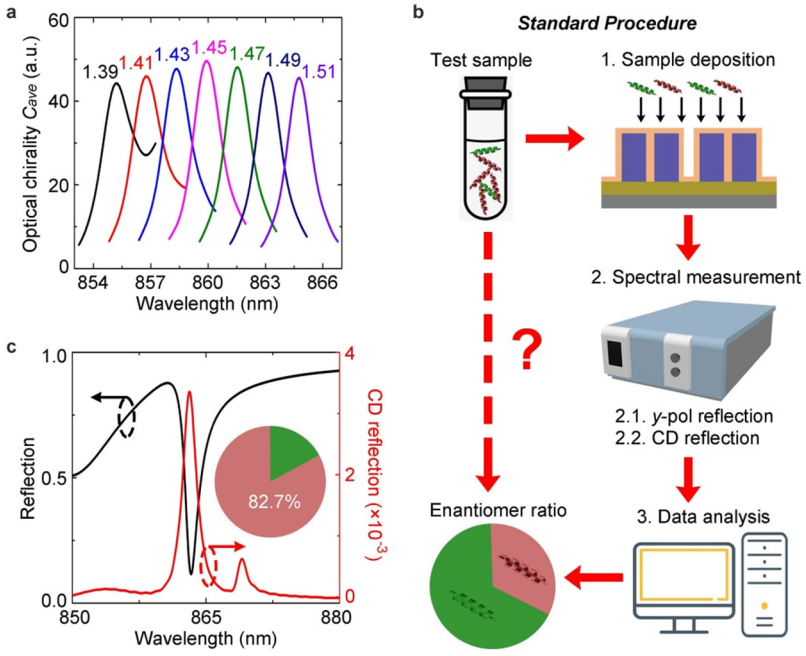

Figure 5. Data analysis and standard procedure for molar chiral sensing. (a) C_{ave} spectra of the metasurface (h = 445 nm) for different RI values of the chiral layer. (b) Standard procedure of molar chiral sensing based on the nanophotonic platform for the acquisition of enantiomer ratio ρ. (c) A typical data set of reflection spectrum and CD reflection spectrum based on which the enantiomer ratio ρ of the sample can be derived.

first fix the molar concentration as M = 0.0133 mol/cm^{-3}. When the chiral sample is purely composed of D-enantiomers (ρ = 100%), κ is calculated to be $(1.52-7.8i) \times 10^{-5}$. As shown in Figure 3e, the ΔR_m spectrum is peaked at 860 nm, corresponding to the C_{ave} resonance. The maximum CD reflection can be as large as 4.45×10^{-3}, which is 69-times stronger than that of a bare chiral layer. This is the largest enhancement in chiral sensing ever achieved to our best knowledge. Besides, since the metasurface itself is structurally achiral and has no chiroptical effects the obtained CD signal totally comes from the chiral molecules. Moreover, the peak value of CD reflection ΔR_m^{peak} follows a linear dependence on κ (Figure 3f). Thus, the metasurface can extract the κ value of chiral sample with high sensitivity.

For the purpose of RI sensing, the variation of environmental RI Δn is detected by the spectral shift of optical resonance $\Delta\lambda$ with a detection sensitivity of $S = \Delta\lambda/\Delta n$.[42] The overall FOM is evaluated by FOM = S/fwhm, where fwhm is the full width at half-maximum of the resonance. Accordingly, the quasi-BIC with a sharp Fano feature provides an ideal candidate for RI sensing. Here, y-polarized reflection spectrum is adopted (see Supporting Information S9) and fitted by the analytical function of Fano resonance F(λ)[43]

$$F(\lambda) = 1 - \frac{a^2}{1 + \left(\frac{\lambda^2 - \lambda_0^2}{2\gamma_0\lambda_0}\right)^2} \frac{b + \left(q + \frac{\lambda^2 - \lambda_f^2}{2\gamma_f\lambda_f}\right)^2}{1 + \left(\frac{\lambda^2 - \lambda_f^2}{2\gamma_f\lambda_f}\right)^2} \quad (11)$$

where a, λ_0, and γ_0 are the amplitude, resonance wavelength ,and width of the broadband mode, respectively, and λ_f, γ_f, q, and b are the resonance wavelength, width, asymmetry parameter, and modulation damping parameter of the Fano resonance, respectively. The fwhm of the Fano resonance is extracted to be γ_f = 1.00 nm (Figure 4a). When the RI of chiral layer is increased, the Fano line shape is preserved and red-shifted as depicted in Figure 4b. The sensitivity is derived to be S = 80.6 nm/RIU (Figure 4c), leading to an FOM of 80.6. Such an FOM sets an inherent detection resolution of about 9.4×10^{-4} mol/cm^3 for the measurement of molecular concentration. Considering the small thickness of the chiral layer (20 nm), the achieved FOM is larger than most of the

https://dx.doi.org/10.1021/acs.nanolett.0c03506
Nano Lett. 2020, 20, 8696−8703

existing works.[20−23] Once the spectral position of quasi-BIC mode is experimentally acquired, the refractive index n of the chiral layer, as well as the permittivity ε_m, is directly retrieved.

When the functions of chiral sensing and RI sensing are integrated on an individual platform, their mutual crosstalk should be considered. In fact, the value of κ has no effect on the spectral position of reflection resonance.[1] Thus, we can extract ε_m by RI sensing without any information about κ and then derive the molar concentration of molecules M among the test sample. The influence of RI dispersion caused by molecular electronic transitions can be ignored (see Supporting Information S10). On the other hand, the variation of ε_m can lead to unequal spectral shifts of x- and y-polarized quasi-BIC modes due to the anisotropy of the metasurface, which will further affect the magnitude of superchiral fields C_{ave}. As shown in Figure 5a, the peak value of C_{ave} is slowly decreased when RI is deviated from 1.45. Although the maximum alternation over the range is not high (∼10%), it should be compensated when calculating κ. It is noted that the dispersion of κ is very weak in this wavelength range and can also be ignored (see Supporting Information S10).

Based on the metasurface, a standard procedure can be established for the integrated acquisition of the enantiomer ratio of a chiral sample (Figure 5b). The test sample is first deposited on the metasurface using molecular thermal evaporation (MTE)[41] or other methods. Then, the metasurface is examined by spectrometer for the measurement of reflection spectrum and CD reflection spectrum. Afterward, the raw spectral data are processed to obtain the enantiomer ratio ρ and molecular concentration M. Figure 5c shows a typical spectral data set based on retrieving M = 0.0164 mol/cm^3 and ρ = 82.7% (for more cases see Supporting Information S11). This procedure possesses apparent advantages over the conventional method. Only one sample needs be prepared, and the required sample volume is quite low. The detection sensitivity is enhanced for the accurate calibration of enantiomer composition, which is important for drug safety and early diagnosis of diseases. Also, all the measurements are conducted over a spectrometer, making the inspection process rapid, cost-effective, and convenient. In addition, the metasurface-based platform has the potential to be integrated with microfluidics for portable detection.[44] Moreover, although the CD signals in this work stem from the molecular electronic transitions, we envision that the proposed metasurface-based approach can also be utilized for the integrated acquisition of molar vibrational CD signals. The excitation wavelengths for vibration transitions usually lie in the infrared spectrum[45] and thus are more accessible by the metasurface.

To summarize, we have theoretically demonstrated a high-Q metasurface for the integrated molar chiral sensing of the enantiomer ratio of a chiral sample with high sensitivity. Because of the simultaneous excitation of x- and y-polarized quasi-BICs with well-matched field distributions, strong superchiral fields are generated, enabling a high enhancement of the CD reflection signal from chiral molecules. Meanwhile, a high FOM is achieved for the RI-based detection of molar molecular concentration. The obtained spectral data is comprehensively analyzed with their cross-talk considered, so that the enantiomer ratio ρ is extracted for the test chiral sample. On the basis of this, a standard procedure is established for the rapid, convenient, economic, and highly sensitive acquisition of enantiomer composition, which promises potential applications in pharmacology, medical diagnostics, and agrochemical industry.

■ ASSOCIATED CONTENT

Supporting Information

The Supporting Information is available free of charge at https://pubs.acs.org/doi/10.1021/acs.nanolett.0c03506.

Simulation details, dispersion of RI and Pasteur parameter κ for chiral molecules, strong coupling between the SLR and TD mode, multipolar decomposition of toroidal dipole, simulations of the TiO_2 dimer metasurface without a gold substrate, analysis of the x-polarized BIC, height-dependent reflection spectra for circularly polarized incidence, origin of the optical chirality resonances, reflection spectra of the metasurface for x-, y-, and circularly polarized light, measurement error of RI and κ caused by their dispersion and another two cases of molar chiral sensing (PDF)

■ AUTHOR INFORMATION

Corresponding Author

Cheng-wei Qiu − *Department of Electrical and Computer Engineering, National University of Singapore, Singapore 117583 Singapore;* orcid.org/0000-0002-6605-500X; Email: eleqc@nus.edu.sg

Authors

Yang Chen − *Department of Electrical and Computer Engineering, National University of Singapore, Singapore 117583 Singapore;* orcid.org/0000-0002-8501-5417

Chen Zhao − *Department of Electrical and Computer Engineering, National University of Singapore, Singapore 117583 Singapore; College of Materials Science and Engineering and Key Laboratory of Advanced Functional Materials, Ministry of Education of China, Beijing University of Technology, Beijing 100124, China*

Yongzhe Zhang − *College of Materials Science and Engineering and Key Laboratory of Advanced Functional Materials, Ministry of Education of China, Beijing University of Technology, Beijing 100124, China;* orcid.org/0000-0002-3471-4402

Complete contact information is available at: https://pubs.acs.org/10.1021/acs.nanolett.0c03506

Author Contributions

Y.C. and C.W.Q. conceived the idea. Y.C. and C.Z. performed the numerical calculations. All authors have analyzed and discussed the results. Y.C. wrote the paper with input from all authors. C.W.Q. supervised the project.

Notes

The authors declare no competing financial interest.

■ ACKNOWLEDGMENTS

C.-W.Q. acknowledges the support from the National Research Foundation, Prime Minister's Office, Singapore, under its Competitive Research Programme (CRP award NRF CRP22-2019-0006).

■ REFERENCES

(1) Barron, L. D. *Molecular light scattering and optical activity*; Cambridge University Press: Cambridge, 2004.

(2) Brenna, E.; Fuganti, C.; Serra, S. Enantioselective perception of chiral odorants. *Tetrahedron: Asymmetry* **2003**, *14*, 1−42.
(3) Abdel-Megied, A. M.; Hanafi, R. S.; Aboul-Enein, H. Y. A chiral enantioseparation generic strategy for anti-Alzheimer and antifungal drugs by short end injection capillary electrophoresis using an experimental design approach. *Chirality* **2018**, *30*, 165−176.
(4) Agranat, I.; Caner, H.; Caldwell, J. Putting chirality to work: the strategy of chiral switches. *Nat. Rev. Drug Discovery* **2002**, *1*, 753.
(5) Kelly, S. M.; Jess, T. J.; Price, N. C. How to study proteins by circular dichroism. *Biochim. Biophys. Acta, Proteins Proteomics* **2005**, *1751*, 119−139.
(6) Greenfield, N. J. Using circular dichroism spectra to estimate protein secondary structure. *Nat. Protoc.* **2006**, *1*, 2876−2890.
(7) Hendry, E.; Carpy, T.; Johnston, J.; Popland, M.; Mikhaylovskiy, R. V.; Lapthorn, A. J.; Kelly, S. M.; Barron, L. D.; Gadegaard, N.; Kadodwala, M. Ultrasensitive detection and characterization of biomolecules using superchiral fields. *Nat. Nanotechnol.* **2010**, *5*, 783−787.
(8) Nesterov, M. L.; Yin, X.; Schäferling, M.; Giessen, H.; Weiss, T. The Role of Plasmon-Generated Near Fields for Enhanced Circular Dichroism Spectroscopy. *ACS Photonics* **2016**, *3*, 578−583.
(9) Zhao, Y.; Askarpour, A. N.; Sun, L.; Shi, J.; Li, X.; Alu, A. Chirality detection of enantiomers using twisted optical metamaterials. *Nat. Commun.* **2017**, *8*, 14180.
(10) Kneer, L. M.; Roller, E. M.; Besteiro, L. V.; Schreiber, R.; Govorov, A. O.; Liedl, T. Circular Dichroism of Chiral Molecules in DNA-Assembled Plasmonic Hotspots. *ACS Nano* **2018**, *12*, 9110−9115.
(11) Yao, K.; Liu, Y. Enhancing circular dichroism by chiral hotspots in silicon nanocube dimers. *Nanoscale* **2018**, *10*, 8779−8786.
(12) Mohammadi, E.; Tsakmakidis, K. L.; Askarpour, A. N.; Dehkhoda, P.; Tavakoli, A.; Altug, H. Nanophotonic Platforms for Enhanced Chiral Sensing. *ACS Photonics* **2018**, *5*, 2669−2675.
(13) Solomon, M. L.; Hu, J.; Lawrence, M.; García-Etxarri, A.; Dionne, J. A. Enantiospecific Optical Enhancement of Chiral Sensing and Separation with Dielectric Metasurfaces. *ACS Photonics* **2019**, *6*, 43−49.
(14) Hu, J.; Lawrence, M.; Dionne, J. A. High Quality Factor Dielectric Metasurfaces for Ultraviolet Circular Dichroism Spectroscopy. *ACS Photonics* **2020**, *7*, 36−42.
(15) Mohammadi, E.; Tavakoli, A.; Dehkhoda, P.; Jahani, Y.; Tsakmakidis, K. L.; Tittl, A.; Altug, H. Accessible Superchiral Near-Fields Driven by Tailored Electric and Magnetic Resonances in All-Dielectric Nanostructures. *ACS Photonics* **2019**, *6*, 1939−1946.
(16) Gilroy, C.; Hashiyada, S.; Endo, K.; Karimullah, A. S.; Barron, L. D.; Okamoto, H.; Togawa, Y.; Kadodwala, M. Roles of Superchirality and Interference in Chiral Plasmonic Biodetection. *J. Phys. Chem. C* **2019**, *123*, 15195−15203.
(17) Yao, K.; Zheng, Y. Near-ultraviolet dielectric metasurfaces: from surface-enhanced circular dichroism spectroscopy to polarization-preserving mirrors. *J. Phys. Chem. C* **2019**, *123*, 11814−11822.
(18) Garcia-Guirado, J.; Svedendahl, M.; Puigdollers, J.; Quidant, R. Enhanced Chiral Sensing with Dielectric Nanoresonators. *Nano Lett.* **2020**, *20*, 585−591.
(19) Chen, Y.; Gao, J.; Yang, X. Chiral Metamaterials of Plasmonic Slanted Nanoapertures with Symmetry Breaking. *Nano Lett.* **2018**, *18*, 520−527.
(20) Offermans, P.; Schaafsma, M. C.; Rodriguez, S. R.; Zhang, Y.; Crego-Calama, M.; Brongersma, S. H.; Gomez Rivas, J. Universal scaling of the figure of merit of plasmonic sensors. *ACS Nano* **2011**, *5*, 5151−5157.
(21) Cetin, A. E.; Altug, H. Fano resonant ring/disk plasmonic nanocavities on conducting substrates for advanced biosensing. *ACS Nano* **2012**, *6*, 9989−9995.
(22) Bahramipanah, M.; Dutta-Gupta, S.; Abasahl, B.; Martin, O. J. Cavity-Coupled Plasmonic Device with Enhanced Sensitivity and Figure-of-Merit. *ACS Nano* **2015**, *9*, 7621−7633.
(23) Davis, M. S.; Zhu, W.; Xu, T.; Lee, J. K.; Lezec, H. J.; Agrawal, A. Aperiodic nanoplasmonic devices for directional colour filtering and sensing. *Nat. Commun.* **2017**, *8*, 1347.
(24) Sreekanth, K. V.; Alapan, Y.; ElKabbash, M.; Ilker, E.; Hinczewski, M.; Gurkan, U. A.; De Luca, A.; Strangi, G. Extreme sensitivity biosensing platform based on hyperbolic metamaterials. *Nat. Mater.* **2016**, *15*, 621−627.
(25) Hsu, C. W.; Zhen, B.; Stone, A. D.; Joannopoulos, J. D.; Soljačić, M. Bound states in the continuum. *Nature Reviews Materials* **2016**, 1.
(26) Tittl, A.; Leitis, A.; Liu, M.; Yesilkoy, F.; Choi, D. Y.; Neshev, D. N.; Kivshar, Y. S.; Altug, H. Imaging-based molecular barcoding with pixelated dielectric metasurfaces. *Science* **2018**, *360*, 1105−1109.
(27) Koshelev, K.; Lepeshov, S.; Liu, M.; Bogdanov, A.; Kivshar, Y. Asymmetric Metasurfaces with High-Q Resonances Governed by Bound States in the Continuum. *Phys. Rev. Lett.* **2018**, *121*, 193903.
(28) Lawrence, M.; Barton, D. R.; Dixon, J.; Song, J.-H.; van de Groep, J.; Brongersma, M. L.; Dionne, J. A. High quality factor phase gradient metasurfaces. *Nat. Nanotechnol.* **2020**, 1−6.
(29) Govorov, A. O.; Fan, Z. Theory of chiral plasmonic nanostructures comprising metal nanocrystals and chiral molecular media. *ChemPhysChem* **2012**, *13*, 2551−2560.
(30) Abdulrahman, N. A.; Fan, Z.; Tonooka, T.; Kelly, S. M.; Gadegaard, N.; Hendry, E.; Govorov, A. O.; Kadodwala, M. Induced chirality through electromagnetic coupling between chiral molecular layers and plasmonic nanostructures. *Nano Lett.* **2012**, *12*, 977−983.
(31) Khorasaninejad, M.; Chen, W. T.; Devlin, R. C.; Oh, J.; Zhu, A. Y.; Capasso, F. Metalenses at visible wavelengths: Diffraction-limited focusing and subwavelength resolution imaging. *Science* **2016**, *352*, 1190−1194.
(32) Azzam, S. I.; Shalaev, V. M.; Boltasseva, A.; Kildishev, A. V. Formation of Bound States in the Continuum in Hybrid Plasmonic-Photonic Systems. *Phys. Rev. Lett.* **2018**, *121*, 253901.
(33) Kravets, V. G.; Kabashin, A. V.; Barnes, W. L.; Grigorenko, A. N. Plasmonic Surface Lattice Resonances: A Review of Properties and Applications. *Chem. Rev.* **2018**, *118*, 5912−5951.
(34) Papasimakis, N.; Fedotov, V. A.; Savinov, V.; Raybould, T. A.; Zheludev, N. I. Electromagnetic toroidal excitations in matter and free space. *Nat. Mater.* **2016**, *15*, 263−271.
(35) Kaelberer, T.; Fedotov, V. A.; Papasimakis, N.; Tsai, D. P.; Zheludev, N. I. Toroidal dipolar response in a metamaterial. *Science* **2010**, *330*, 1510−1512.
(36) Xu, L.; Rahmani, M.; Zangeneh Kamali, K.; Lamprianidis, A.; Ghirardini, L.; Sautter, J.; Camacho-Morales, R.; Chen, H.; Parry, M.; Staude, I.; Zhang, G.; Neshev, D.; Miroshnichenko, A. E. Boosting third-harmonic generation by a mirror-enhanced anapole resonator. *Light: Sci. Appl.* **2018**, *7*, 44.
(37) Semmlinger, M.; Zhang, M.; Tseng, M. L.; Huang, T. T.; Yang, J.; Tsai, D. P.; Nordlander, P.; Halas, N. J. Generating Third Harmonic Vacuum Ultraviolet Light with a TiO2Metasurface. *Nano Lett.* **2019**, *19*, 8972−8978.
(38) Miroshnichenko, A. E.; Evlyukhin, A. B.; Kivshar, Y. S.; Chichkov, B. N. Substrate-Induced Resonant Magnetoelectric Effects for Dielectric Nanoparticles. *ACS Photonics* **2015**, *2*, 1423−1428.
(39) Tang, Y.; Cohen, A. E. Optical chirality and its interaction with matter. *Phys. Rev. Lett.* **2010**, *104*, 163901.
(40) Tang, Y.; Cohen, A. E. Enhanced enantioselectivity in excitation of chiral molecules by superchiral light. *Science* **2011**, *332*, 333−336.
(41) García-Guirado, J.; Svedendahl, M.; Puigdollers, J.; Quidant, R. Enantiomer-selective molecular sensing using racemic nanoplasmonic arrays. *Nano Lett.* **2018**, *18*, 6279−6285.
(42) Anker, J. N.; Hall, W. P.; Lyandres, O.; Shah, N. C.; Zhao, J.; Van Duyne, R. P. Biosensing with plasmonic nanosensors. *Nat. Mater.* **2008**, *7*, 442−453.
(43) Gallinet, B.; Martin, O. J. Influence of electromagnetic interactions on the line shape of plasmonic Fano resonances. *ACS Nano* **2011**, *5*, 8999−9008.

https://dx.doi.org/10.1021/acs.nanolett.0c03506
Nano Lett. 2020, 20, 8696−8703

(44) Yavas, O.; Svedendahl, M.; Dobosz, P.; Sanz, V.; Quidant, R. On-a-chip Biosensing Based on All-Dielectric Nanoresonators. *Nano Lett.* **2017**, *17*, 4421−4426.
(45) Collins, J. T.; Kuppe, C.; Hooper, D. C.; Sibilia, C.; Centini, M.; Valev, V. K. Chirality and Chiroptical Effects in Metal Nanostructures: Fundamentals and Current Trends. *Adv. Opt. Mater.* **2017**, *5*, 1700182.

https://dx.doi.org/10.1021/acs.nanolett.0c03506
Nano Lett. 2020, 20, 8696−8703